TUDelft

Delft University of Technology

Monitoring spatiotemporal variation in beach surface moisture using a long-range terrestrial laser scanner

Jin, Junling ; Verbeurgt, Jeffrey; De Sloover, Lars; Stal, Cornelis; Deruyter, Greet; Montreuil, Anne-Lise; Vos, Sander; de Maeyer, Philippe; De Wulf, Alain

Citation (APA)
Jin, J., Verbeurgt, J., De Sloover, L., Stal, C., Deruyter, G., Montreuil, A.-L., Vos, S., de Maeyer, P., & De Wulf, A. (2021). Monitoring spatiotemporal variation in beach surface moisture using a long-range terrestrial laser scanner. *ISPRS Journal of Photogrammetry and Remote Sensing*, *173*, 195-208. https://doi.org/10.1016/j.isprsjprs.2021.01.011

Important note
To cite this publication, please use the final published version (if applicable).
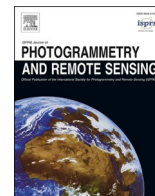Please check the document version above.

Monitoring spatiotemporal variation in beach surface moisture using a long-range terrestrial laser scanner

Junling Jin [a],[*], Jeffrey Verbeurgt [a], Lars De Sloover [a], Cornelis Stal [a],[b], Greet Deruyter [c], Anne-Lise Montreuil [d], Sander Vos [e], Philippe De Maeyer [a], Alain De Wulf [a]

[a] *Department of Geography, Ghent University, Krijgslaan 281 S8, 9000 Ghent, Belgium*
[b] *Department of Real-estate and Applied Geomatics, University College Ghent, Valentin Vaerwyckweg 1, 9000 Ghent, Belgium*
[c] *Department of Civil Engineering, Ghent University, Technologiepark 904, 9052 Ghent, Belgium*
[d] *Hydrology and Hydraulic Engineering, Vrije Universiteit Brussel, Pleinlaan 2, 1050 Elsene, Belgium*
[e] *Department of Hydraulic Engineering, Delft University of Technology, Delft, the Netherlands*

ABSTRACT

The measurement of surface moisture on beaches is vital for studying aeolian sand transport mechanisms, but existing techniques are not adequate for monitoring the surface moisture dynamics over a substantial beach section. In this study, we investigated the suitability of a new remote sensing method to monitor the spatio-temporal variation in surface moisture on a sandy beach using a long-range static terrestrial laser scanner (TLS). The TLS was permanently deployed on top of a 42 m high building overlooking the study site at Ostend-Mariakerke, Belgium. Considering the effect of target surface roughness on the intensity and the laboratory's length limitation, a new intensity correction method is proposed which only uses the field point cloud data measured on a homogenous beach surface (without time-consuming indoor experiments). Based on the corrected intensity data, the relation of the beach surface moisture to the corrected intensity was modeled by an exponential model with a correlation-coefficient squared of 0.92. A moisture estimation model was developed which can directly derive the beach surface moisture from the original intensity data of the TLS with a standard error of 2.27%. The hourly surface moisture dynamics across two tidal cycles on the beach were investigated as a case study, in which the point clouds derived from corresponding unmanned aerial vehicle (UAV) imagery are utilized to improve the calculation accuracy of the incidence angles of TLS point clouds at long distances. Results reveal that, after the intensity correction, the long-range static TLS is an extremely suitable technique to monitor the surface moisture dynamics (daytime and nighttime) over a substantial beach section (hundreds of meters) at a high scanning frequency (minutes to hours).

1. Introduction

The aeolian sand transport on beaches is the main sediment source into coastal dunes, which helps the dune recover from the erosion effects of storm-wave processes and grow during prolonged gentle weather conditions (Bauer et al., 2009; Brakenhoff et al., 2019; Oblinger and Anthony, 2008; Smit et al., 2018). However, the present prediction models for the aeolian sand transport mainly depend on wind characteristics, in which the measured sand supply to dunes is generally considerably less than the model predictions (Delgado-Fernandez, 2011; Keijsers et al., 2016). The beach surface moisture is considered as the key supply-limiting factor. Surface moisture content increases the resistance of the uppermost sand layer to be entrained by the wind and reduces the aeolian transport rate by the adhesive forces within wet sand grains (Davidson-Arnott et al., 2008). When the surface moisture exceeds a threshold, about 10% gravimetric moisture content, the aeolian transport is entirely prohibited (Smit et al., 2019). However, the surface moisture is often highly dynamic over space and time due to the synthetic effect of the beach terrain, tide, groundwater, precipitation and evaporation, etc. (Atherton et al., 2001; Namikas et al., 2010) and it is thus very challenging to parameterize. This has prevented the development of quantitatively more realistic aeolian sand transport models over substantial beach sections.

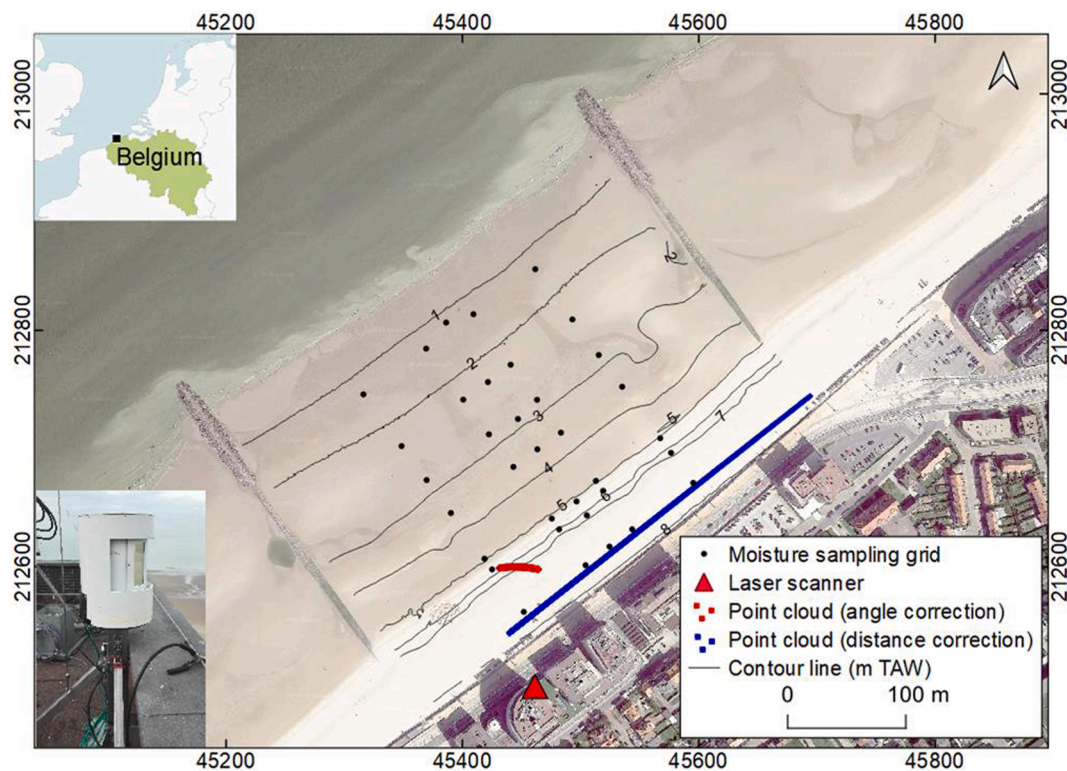Traditionally, the beach surface moisture was measured based on

---

Fig. 1. Field deployment at the beach of Ostend-Mariakerke and the surface moisture sampling grid (black points). Insets: location of the study site and set-up of the Riegl VZ-2000 TLS.

spot-based sampling methods, including using soil moisture probes, handheld spectroradiometer, sample gravimetric measurements, etc. (Davidson-Arnott et al., 2008; Edwards and Namikas, 2009; Edwards et al., 2013; Namikas et al., 2010; Wiggs et al., 2004). These methods mainly provide a scattering of points representing a beach fraction. It is difficult to analyze the surface moisture contents at high spatial and temporal resolution unless significant quantities of field observation data are available, which is laborious, costly and time-consuming (Yang et al., 2019). In contrast, the optical remote sensing methods hold great promise for rapidly measuring the surface moisture over a substantial section of beach in a non-contact way. These methods usually employ visible, near-infrared (NIR) and shortwave infrared (SWIR) wavelengths, in which the SWIR wavelengths are more sensitive to the target moisture variation than the visible and NIR wavelengths, due to stronger energy absorption in water (Yang et al., 2019). The common optical brightness methods (using a video system) only work during daytime and require a brightness compensation for the changing ambient light and therefore yield a lower measurement accuracy (Darke et al., 2009; Delgado-Fernandez and Davidson-Arnott, 2011; McKenna Neuman and Langston, 2006; Montreuil et al., 2018). In contrast, terrestrial laser scanning (TLS) is a more promising remote sensing technique, which can measure both the beach morphology and surface moisture variation with a high spatiotemporal resolution. In addition, as an active remote sensing technique, TLS is not affected by the changing ambient light (Nield et al., 2014; Nield and Wiggs, 2011; Ruessink et al., 2014). Based on the radar equation, the TLS original intensity can be calibrated to the beach surface reflectance which is closely related to surface moisture contents assuming that the other beach surface properties (the surface roughness and the sand grain size, etc.) remain unchanged (Nolet et al., 2014; Smit et al., 2018).

Several studies have already demonstrated the potential of estimating the sandy beach surface moisture using the short-range TLS (e.g., Leica Scanstation 2) (Nield et al., 2014; Nield and Wiggs, 2011; Nield et al., 2011) and the middle-range TLS (e.g., Riegl VZ-400) (Ruessink

et al., 2014; Smit et al., 2019; Smit et al., 2018). However, the scanning range effect on the TLS backscattered intensity was eliminated only with a $1/R^2$ correction (ignoring the impact of the near-range reducer) and the incidence angle effect was also ignored (Jin et al., 2020). Additionally, the maximum measured distances of these laser scanners are quite small (tens of meters) because of the limitation of the transmitting energy and scanner height. Recently, a mobile terrestrial LiDAR system (MTL) was tested using a Kymco all-terrain vehicle with a short-range TLS (Z&F/Leica HDS6100) for the larger-area beach surface moisture measurement (Jin et al., 2020). Nonetheless, this method is labor-intensive and the tracks of the all-terrain vehicle itself disturbed the beach surface to some extent. Tan (Tan et al., 2020) attempted to estimate the water contents of intertidal mudflats utilizing a long-range TLS (Riegl VZ-4000), in which the water content of the mudflats was generally higher than those of sandy beaches, and numerous indoor and outdoor experiments were carried out for the intensity calibration.

In this study, we investigate the suitability of a long-range static TLS (Riegl VZ-2000) to monitor the spatiotemporal variation in surface moisture on a sandy beach. The proposed method is meaningful in the studies of the coastal aeolian sand transport, the distribution of the beach groundwater and coastal ecosystem, etc. After a brief introduction of the study site, the used instruments and data collection are described (Section 2). Subsequently, the theory for surface moisture estimation is briefly outlined and a new intensity correction method is proposed which only utilizes the field point cloud data measured on a homogenous beach surface without time-consuming indoor experiments (Section 3). Next, the correction results are presented (Section 4). The hourly surface moisture dynamics across two tidal cycles on the beach were investigated as a case study, in which the point clouds derived from corresponding unmanned aerial vehicle (UAV) imagery are utilized to improve the calculation accuracy of the incidence angles of TLS point clouds at long distances (Section 5). Section 6 formulates the conclusions.

Table 1
Main parameters of the Riegl VZ-2000.

Attribute	Value
Wavelength	1550 nm
Range	2.5–2050 m
Field of View	360° × 100°
Laser beam divergence	0.3 mrad
Accuracy	8 mm (at 150 m range)
Precision	5 mm (at 150 m range)
Vertical/Horizontal Angular Step	0.0015–1.15°
	0.0024–0.62°

2. Study site and data collection

2.1. Study site

The measurements were conducted at Ostend-Mariakerke (51.213° N, 2.872° E), along the Belgian coast (Fig. 1). It is a relatively wide (exceeds 200 m during low tide) and dissipative sandy beach with a low slope (2°) (Montreuil et al., 2018). The study area is typically macrotidal with a spring tide of 5 m and a neap tide of 3.5 m (Deronde et al., 2008). The sediment predominantly consists of quartz sand with a fine and medium range: the sand grain size slightly increases from the backshore (D_{50} = 291 μm) to the lower intertidal zone (D_{50} = 337 μm) (Montreuil et al., 2018).

The climate is mild with an average annual temperature of 10.6 °C and an average rainfall of about 748 mm. The predominant wind direction comes from the southwest with speeds of 3–8 m/s (Montreuil et al., 2018). The nearshore environment is low energy with typical wave heights of about 0.5–1 m (Haerens et al., 2012). There are neither buildings nor vegetation on the beach, but the area is often frequented by people leaving footsteps and tire tracks in the sand.

2.2. Riegl VZ-2000 TLS

The measurements were performed using a long-range Riegl VZ-2000 TLS (Table 1), which utilizes a shortwave near-infrared (1550 nm) laser. The vertical and horizontal fields of view are 100° and 360°, respectively. It should be noted that theoretically, the maximum measured distance of the Riegl VZ-2000 TLS is up to 2050 m (when the albedo ≥ 90%), and the accuracy and precision are up to 8 mm and 5 mm, respectively (at 150 m under Riegl test conditions). However, it is difficult to be achieved in actual scans, especially in the case of scanning on a wet beach. The raw coordinates (x, y and z) of the point clouds were relative to the scanner center, which were converted into the local coordinate system by means of the reflectors (positioning with an RTK-GPS) placed on the beach. In the present study, as this research is part of the Belgian CREST Project (VLIZ, 2020), we adopted the Belgian Lambert 72 (EPSG: 31 370) coordinate reference system and the TAW (Tweede Algemene Waterpassing) (Ostend Height, EPSG: 5 110) reference level. Considering the study area is relatively small, the distance and angle deviation caused by the adopted coordinate reference system was ignored (Kuschnerus et al., 2020; Yang et al., 2020). The backscattered intensity was recorded as a dimensionless number.

The scanner was permanently deployed on top of a high building (about 42 m) overlooking the target beach at Ostend-Mariakerke from November 2017 to December 2018 (De Sloover et al., 2019). The study site was scanned hourly to detect the variation of beach morphology and surface moisture. The scanner was shielded by a custom-made all-weather protective housing thus reducing the horizontal field of view to 200°. A command computer with attached storage was employed to steer the scanner, in which a task scheduler was run to automatically instruct an hourly scan under all weather conditions (Vos et al., 2017). The duration of each scan lasted for about 4 min.

2.3. Data collection

The surface moisture samples were manually collected at an established sampling grid (Fig. 1). The sampling grid comprised 5 alongshore transects (each transect was composed of 7 points), extending from the upper-beach to the dissipative intertidal area. The size of each moisture sample was approximately 10 × 10 cm, and the thickness was about 0.5 cm. An RTK-GPS system was used to determine the accurate location of the center of each moisture sample. The gravimetric moisture contents of these field samples were analyzed in the laboratory by calculating the ratio of the water weight in the sample to the weight of the wet sample (Nield and Wiggs, 2011; Smit et al., 2018). A total of 114 moisture samples were collected after the TLS scanning at low tide from April 18th to April 26th, 2018. It is noteworthy that several points of the sampling grid were inundated with very shallow water when sampling but the dense point cloud data were still collected in these areas. In this study, it was assumed that the moisture samples in these areas were saturated. Furthermore, some important parameters thought to influence the surface moisture contents were also simultaneously collected from nearby weather stations (Coast, 2020), including the air temperature, precipitation, wind speed/direction, solar radiation intensity, air relative humidity, groundwater table and tidal elevation. It is noteworthy that the dipwell was not perfectly located at the study site. There were two breakwaters between the dipwell and the study site (about 600 m). Thus, its data are only used as a reference.

3. Theory and methods

3.1. Surface moisture – intensity model

Previous studies have shown that it is possible to derive the beach surface moisture from the corrected backscattered intensity when other beach surface properties remain constant (Jin et al., 2020; Nield et al., 2014; Philpot, 2010; Smit et al., 2018; Tan et al., 2020). In this study, the relation was expressed using an exponential model which is similar to the studies of Jin et al. (2020) and Tan et al. (2020).

$$I_c = F_1(M) = \delta e^{cM} \tag{1}$$

Here I_c denotes the corrected TLS intensity (independent to the range and incidence angle) and M is the beach surface moisture content. δ and c are two constants which are determined by the laser wavelength and sand properties. However, the original intensity data need to be corrected to eliminate the scanning geometry effect for deriving the moisture contents (Fang et al., 2015; Kaasalainen et al., 2011; Smit et al., 2018). Based on the radar equation, the impact of the range and incidence angle on the backscattered intensity is independent of each other and can be corrected separately by regression analysis (Fang et al., 2015; Jin et al., 2020; Tan and Cheng, 2015). Regardless of the effects of the instrumental mechanisms and atmospheric transmission factors, the original backscattered intensity I can be written as:

$$I = F_1(M) \cdot F_2(\cos\theta) \cdot F_3(R) \tag{2}$$

where F_1 is a function of the surface moisture content M, which is proportional to the target surface reflectance. Here, F_1 is expressed using Eq. (1). F_2 and F_3 represent a function of the cosine of the incidence angle $\cos\theta$ and the scanning distance R, respectively. The $\cos\theta$ is derived using:

$$\cos\theta = \left| \frac{v_{ps} \cdot v_n}{R} \right| \tag{3}$$

where v_{ps} denotes the vector from the scanning point to the scanner center. v_n is the unit normal vector of the best-fitting plane computed by the nearby points around each TLS scanning point. According to the Weierstrass approximation theorem (Stone, 1948), the functions $F_2(\cos\theta)$ and $F_3(R)$ can be empirically approximated by the polynomial

$\sum_{i=0}^{N_1}[\beta_i(\cos\theta)^i]$ and $\sum_{i=0}^{N_2}(\gamma_i R^i)$, respectively. Combining Eq. (1) and Eq. (2), this generates:

$$I = \delta e^{cM} \cdot \sum_{i=0}^{N_1}[\beta_i(\cos\theta)^i] \cdot \sum_{i=0}^{N_2}(\gamma_i R^i) \tag{4}$$

Here N_1 and N_2 represent the polynomial order. β_i and γ_i show the polynomial coefficient. The parameters in Equation (4) were estimated using the method introduced in Section 3.2.

In previous studies, the original backscattered intensity is generally corrected to a value proportional (or equal) to the target surface reflectance (Fang et al., 2015; Tan and Cheng, 2015). In this study, the original intensity is converted to the target surface moisture contents directly. The corrected intensities of these two methods are both independent of the incidence angle and the scanning distance. The latter is exponentially related to the surface reflectance, while the former is proportional (or equal) to the target surface reflectance. Thus, the final model of the surface moisture content M is expressed as:

$$M = \frac{1}{c} ln\left(\frac{I}{\delta(\sum_{i=0}^{N_1}[\beta_i(cos\theta)^i] \cdot \sum_{i=0}^{N_2}(\gamma_i R^i))}\right) \tag{5}$$

3.2. Estimation of surface moisture model's parameters

In previous studies, the polynomial parameters of $F_2(\cos\theta)$ in Eq. (4) were determined using commercial target panels with calibrated reflectance, scanned at a fixed range and various incidence angles in the indoor environment (Fang et al., 2015; Tan and Cheng, 2015). However, studies have shown that the target surface's roughness plays a vital role in the effect of the incidence angle on the intensity (Kaasalainen et al., 2009; Kukko et al., 2008; Zámečníková and Neuner, 2017). Considering that the roughness of the real beach surface is generally different from the commercial target panels, the correction experiment should be conducted using real sand samples. However, it is difficult to avoid disturbance of the sand samples' surface owing to the sliding of dry sand grains when placing the sand samples at various incidence angles (Jin et al., 2020). In addition, it may be impractical to remove the scanner which is permanently deployed at the fixed position for the indoor correction experiments.

In this study, instead of using time-consuming indoor correction experiments, the field point clouds acquired at natural homogenous targets are adopted to estimate the polynomial parameters of $F_2(\cos\theta)$. Generally, on a sandy beach with aeolian transport, there are relatively

dry upper-beaches or artificial/natural dunes. The sand within a certain beach area could be considered to have a similar mineral composition, grain size and surface roughness. In this study, the sand grain size (D_{50} = 291 μm) on the upper-beach is almost equal to the grain size in the intertidal zone (D_{50} = 306 μm). Moreover, based on our previous experience and sample checking, the uppermost sand layer in the upper-beach was considered to be dry (<1%) at noon of a sunny day (Jin et al., 2020). As a consequence, the upper-beach (at noon of a sunny day) might be considered as a homogenous target with similar surface properties. In this study, the point cloud data in a very narrow arc-like strip (red) are selected (Fig. 1). These data are located in the known dry upper-beach with similar surface properties, and the distance from the point cloud within this strip to the scanner center is also almost the same, in the range of 113.5–113.9 m (0.4 m width arc-like strip). In these conditions, the scanning distance and surface moisture of this area might be considered as the constants, and thus $F_1(M)$ and $F_3(R)$ are also the constants. In contrast, due to the topographic relief on the upper-beach surface, the incidence angles of the point cloud in the strip are varying. Normally, it is not difficult to get a wide range of the incidence angle on the upper-beach (or artificial/natural dunes) if the used point cloud strip is long enough and the upper-beach is not completely flat. Setting $c_1 = F_1(M) \cdot F_3(R)$, the backscattered intensity I is merely correlated with the incidence angle and is expressed as:

$$I = c_1 \sum_{i=0}^{N_1}[\beta_i(\cos\theta)^i] \tag{6}$$

The values of $c_1\beta_i$ can be estimated using a least-square fitting. The polynomial order N_1 is determined by making an integrative consideration of the accuracy and simplicity of the model. Setting the highest order's coefficient $\beta_{N_1} = 1$ resulted in $c_1 = c_1\beta_{N_1}$ and $\beta_i = c_1\beta_i/c_1$ (Jin et al., 2020; Tan et al., 2019). To reduce possible errors using only one scanning strip, several point cloud strips meeting the conditions should be used and then the average of β_i is obtained as the final coefficient of the polynomial $F_2(\cos\theta)$.

For the determination of the parameters of the polynomial $F_3(R)$, compared with the short-range and middle-range TLS, it is also infeasible to conduct the indoor correction experiments at various scanning distances from meters to kilometers (with a fixed incidence angle) for the long-range TLS, because the indoor environment limits the practical maximum scanning distance. Similarly, the point cloud data in a long narrow strip (1 m width) on the beach are manually sampled to estimate the polynomial parameters of $F_3(R)$ in this study. As shown in Fig. 1, the point cloud strip (blue) is also located in the upper-beach with similar
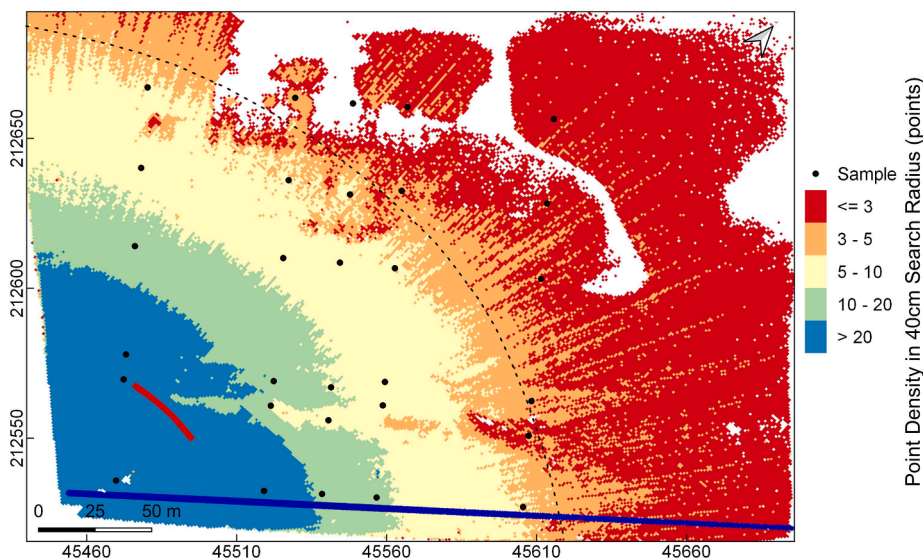

Fig. 2. The density (0.4 m search radius) of the point cloud data of the Riegl VZ-2000 TLS acquired on Ostend-Mariakerke beach on April 18th, 2018 (10:00, low tide). The black dotted line denotes the distance of 250 m from the scanner center. The red and blue strip represent the sampled point cloud data for the incidence angle effect correction and distance effect correction, respectively. (For interpretation of the references to color in this figure legend, the reader is referred to the web version of this article.)
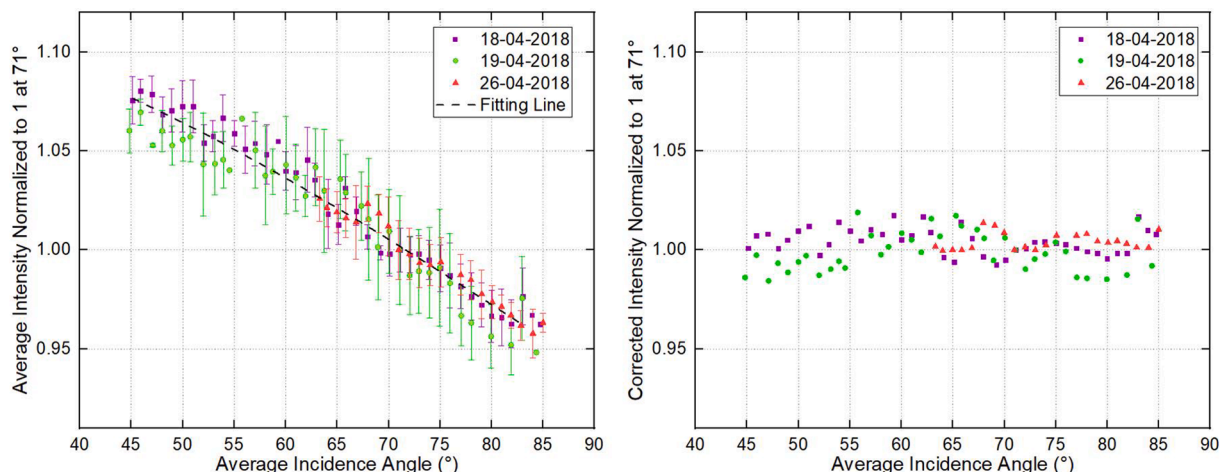
Fig. 3. (a) The average original intensity (normalized to 1 at 71°) vs. the average incidence angles of the point cloud data captured on three dates using a Riegl VZ-2000 TLS. The dashed line denotes the best-fitting line based on Eq. (6). The error bars indicate the intensity standard deviations for each one-degree interval (b) The incidence angle-corrected intensity (normalized to 1 at 71°) vs. the average incidence angles of the three datasets.

surface properties. The distance from the point cloud within the strip to the scanner varies in the range from 60 m to 350 m. The strip length is determined based on the practical requirements of distance correction. Theoretically, the maximum strip length could equal the maximum efficient scanning distance of the TLS if the upper-beach (or artificial/natural dunes) along the shoreline is long enough for the study site.

It is noteworthy that the original intensity of the point cloud data within this strip is affected by both the scanning distance and incidence angle. To estimate the parameters of the polynomial $F_3(R)$, the incidence angle-corrected intensity I_a should be calculated first by dividing the original intensity by $F_2(\cos\theta)$ (with the derived coefficients in Eq. (6)). Afterwards, the incidence angle-corrected intensity I_a is merely correlated with the scanning distance, and independent to the surface moisture and the incidence angle. In these conditions, $F_1(M)$ and $F_2(\cos\theta)$ might be considered as two constants, setting $c_2 = F_1(M) \cdot F_2(\cos\theta)$. The intensity level I_a is expressed as

$$I_a = c_2 \sum_{i=0}^{N_2} (\gamma_i R^i) \qquad (7)$$

Similarly, the value $c_2\gamma_i$ can be estimated using a least-square fitting. The polynomial order N_2 is determined by making an integrative consideration of the accuracy and simplicity of the model. Setting $\gamma_{N_2} = 1$ resulted in $c_2 = c_2\gamma_{N_2}$ and $\gamma_i = c_2\gamma_i/c_2$. To reduce random errors, the average of γ_i should be computed as the final coefficient of the polynomial $F_2(\cos\theta)$ using several point cloud strips meeting the conditions. Furthermore, based on the derived coefficients in Eq. (7), the intensity I_c in the moisture sampling grid can be calculated by dividing the incidence angle-corrected intensity I_a by the $F_3(R)$. Afterwards, the parameters in $F_1(M)$ (Eq. (1)) are estimated by a least-square fitting. Finally, the surface moisture contents on the beach are estimated using Eq. (5) based on the TLS point cloud data.

4. Results and discussion

4.1. Incidence angle effect correction

After preprocessing the point cloud data, an arc-like strip (red) of the point cloud on the upper-beach (Fig. 1) was adopted for the incidence angle effect correction. The arc-like strip had a length of about 35 m and a width of 0.4 m (obtained with MATLAB programming). It is noteworthy that – due to the decrease of point density upon increasing scanning distance as shown in Fig. 2 - the arc-like strip was selected in the near-distance area from the scanner with a scanning distance

between 113.5 m and 113.9 m. Based on the dense nearby points, the plane normal vector of each scanning point (for computing the incidence angle) was derived with a small radius (20 cm). Also, to reduce possible noise using the original point cloud data directly, the average of the intensity and incidence angle was calculated at intervals of one-degree angle for the subsequent incidence angle effect correction. On the other hand, to reduce the possible effect from atmospheric factors, a total of three arc-like strips was sampled in the same position of the upper-beach to obtain the average of the correction parameters. The sampling time was at 14:00–15:00 (with higher sun radiation) of three sunny days (April 18th, 19th and 26th, 2018, see the tide data in Section 5.3). Although the intensity correction was not carried out in an indoor controlled environment, the derived correction parameters are more suitable to the practical field measurement.

The incidence angle effect on the original intensity is shown in Fig. 3a. To compare the intensity vs. the incidence angle behavior of these three datasets more easily, the intensity values were normalized to equal 1 at an incidence angle of 71°. It is noteworthy that the range of incidence angles adopted was not covering the full range of 0° to 90°, but it should meet the practical correction requirements for the point cloud data captured on the beach. If it is difficult to get a wide range of incidence angles in a single point cloud strip on very flat beaches, several point cloud strips at different positions should be sampled for a piece-wise correction and the average of the correction parameters is calculated as the final model parameters. In this study, the correction range of incidence angles should cover at least 54° (61 m) to 85° (400 m), considering the flatness of the beach. Compared with the indoor correction experiments, the changes in incidence angles were more continuous (one-degree interval) in this study, which helps to accurately estimate the incidence angle-intensity relation.

As illustrated in Fig. 3a, the overall tendency between the original backscattered intensity and incidence angles was almost the same for the three datasets captured on different dates. The original intensity decreased gradually with the increasement of the incidence angles in the range of 45° to 85°, which is similar to the experiment result of (Jin et al., 2020). Compared to the experiments in (Kaasalainen et al., 2011; Kukko et al., 2008), the downward trend of the original intensity (versus the increasing incidence angle) was clearer in this study. One possible reason is that the adopted incidence angles (45–85°) are markedly larger than in the cited studies (0–40°). Thus, it is necessary to correct the incidence angle effect before deriving the beach surface moisture from the original intensity data.

Based on the method introduced in Section 3.2, a first-order polynomial (the fitting line in Fig. 3a) was adopted to fit $F_2(\cos\theta)$ after testing

Table 2
Estimated values of the parameters in Eq. (5).

$F_1(M)$	δ	c		
	1.49×10^{-5}	-3.75		
$F_2(\cos\theta)$	N_1	β_0	β_1	
	1	4.79 ± 0.13	1	
$F_3(R)$	N_2	γ_0	γ_1	γ_2
	2	401876.68 ± 20213.45	-1198.95 ± 56.52	1

different orders of polynomials. Three sets of polynomial parameters for $F_2(\cos\theta)$ were estimated by least-square fitting and the average of the three sets of parameters was calculated as the final adopted polynomial parameters (Table 2). The mean correlation-coefficient squared (R^2) was 0.95 ± 0.02. Using the estimated parameters, the incidence angle-corrected intensity of the three sets of point cloud data were calculated by dividing the original intensity by $F_2(\cos\theta)$ and the results were normalized to equal 1 at 71°. As shown in Fig. 3b, after the incidence angle effect correction, the intensity became completely independent of the incidence angles and almost equal to 1 (the intensity value at 71°), with a root mean square error (RMSE) of 0.008.

4.2. Distance effect correction

As shown in Fig. 1, a long narrow strip (blue) of the point cloud data on the upper-beach was manually sampled as the data for the distance effect correction. Normally, the length of the point cloud strips should be sufficiently long to meet the practical correction requirements on the beach. However, sometimes it is difficult to obtain a very long (e.g., 500 m) continuous point cloud strip in the upper-beach. An alternative is to sample in the planned point cloud strip at intervals of several meters. In this study, the distances from the point clouds (within the strip) to the scanner center were 60 m to 350 m, almost covering all possible scanning distances of the field point cloud data on the beach. The plane normal vector of each scanning point (within the blue strip) was derived with a 40 cm radius, considering that the blue strip is situated in a flatter area along the artificial berm based on the contour line shown in Fig. 1. The average of the intensity, distance and incidence angle at 1-m intervals was calculated for the subsequent intensity correction. The average of the intensity standard deviation was 0.02, about 2% of the intensity range of the point cloud strips. A total of three long, narrow strips of point cloud data were sampled on April 18th, 19th and 26th, 2018, from the same TLS scanning data with the red arc-like strip. The impact of the scanning distances on the original intensity is shown in Fig. 4a, in which the intensity values have been normalized to equal 1 at 150 m. It is noteworthy that the change in distance was more continuous and detailed by using the field points cloud data compared with the

indoor correction experiments. The latter was generally carried out from the minimum to the maximum distance at several-meter intervals to estimate the distance vs. the intensity relation (Tan et al., 2019). Here, to show the error bars clearly, the datasets shown in Fig. 4 were made thinner (one point per 5 m), but it did not affect the real datasets used for the distance correction.

Considering the fact that the original backscattered intensity was affected by both the scanning distance and incidence angle, the incidence angle-corrected intensity I_a was calculated first based on the estimated parameters of $F_2(\cos\theta)$ in Section 4.1. As illustrated in Fig. 4b, the overall tendency between the incidence angle-corrected intensity and distance was almost the same for the three datasets captured on different dates, and the incidence angle-corrected intensity monotonically decreased with the increasing scanning distance from 60 m to 350 m. Similar trends were observed in the studies (Ruessink et al., 2014; Smit et al., 2018). Here, the measured beach did not cover the area of scanning distances < 60 m, in which the backscattered intensity at near distances could be affected by the built-in automatic reducers of the scanner (Fang et al., 2015). For this condition, the proposed correction method is also applicable by using a high-order polynomial. It is noteworthy that the slope and curvature of the incidence angle-corrected intensity vs. the distance (Fig. 4b) was slightly smaller than the one of the original intensity vs. the distance (Fig. 4a) due to the elimination of the incidence angle effect. In addition, while comparing Fig. 4b with the Fig. 3a, it is easy to find that the distance has a more serious effect on the intensity than the incidence angle.

Based on the method introduced in Section 3.2, different orders of polynomials were tested, a second-order polynomial (the fitting line in Fig. 4b) was adopted to fit $F_3(R)$ with a mean correlation-coefficient squared of 0.99 ± 0.002. By the least-square fitting, three sets of polynomial coefficients for $F_3(R)$ were estimated and the average of the three sets of parameters was calculated as the final adopted parameters for $F_3(R)$ (Table 2). The final corrected intensity I_c was obtained based on the method introduced in Section 3.2 and normalized to equal 1 at 150 m. As illustrated in Fig. 4c, the final corrected intensity was completely independent of the scanning distance. Most of these intensities were almost equal to 1 (the intensity value at 150 m) with a RMSE of 0.037, except for several points at a long distance.

4.3. Surface moisture estimation

Based on the derived coefficients for Eq. (6) and Eq. (7) in Table 2, we obtained the corrected intensity I_c of the point clouds in a 1×1 m grid cell around each moisture sampling position. The average corrected intensity in each grid cell was calculated to be compared with the corresponding gravimetric moisture contents as shown in Fig. 5a, in which the shown intensity data were normalized to equal 1 at 7.9% moisture.
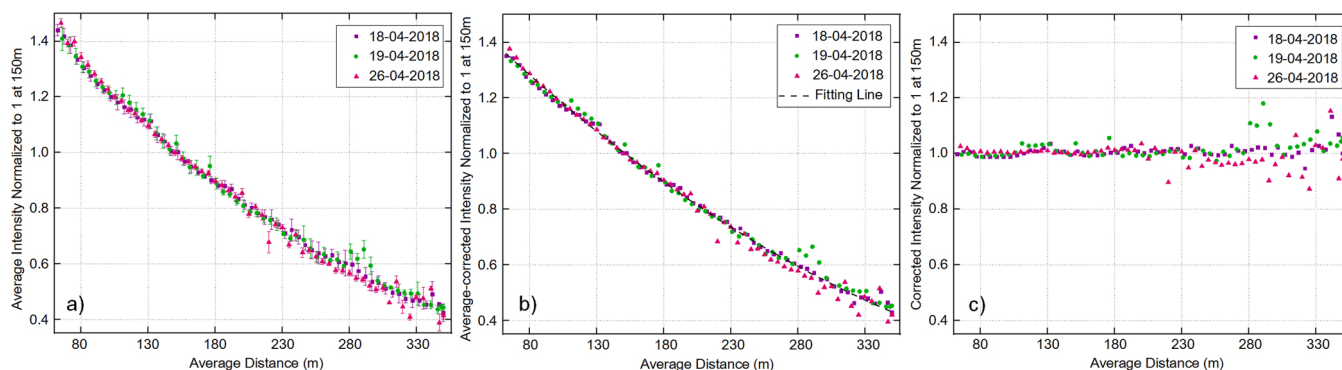

Fig. 4. (a) The average original intensity (normalized to 1 at 150 m) vs. the average distance of the point cloud data captured on three dates using a Riegl VZ-2000 TLS. The error bars indicate the intensity standard deviations for each 1-m interval (b) The incidence angle-corrected intensity vs. the average distance. The dashed line denotes the best-fitting line based on Eq. (7). (c) The final corrected intensity vs. the average distance. The former is independent of both the scanning distance and incidence angle.
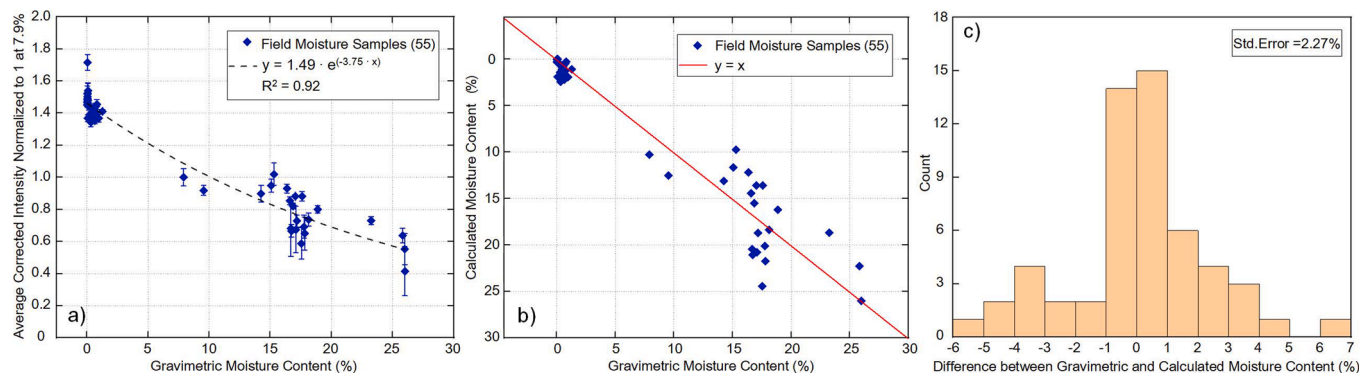
Fig. 5. (a) The gravimetric moisture content vs. the average corrected intensity which is independent of both the incidence angle and scanning distance (normalized to 1 at 7.9% moisture). The error bars indicate the standard deviations of the corrected intensities in each sampling grid cell (1 × 1 m). The dashed line denotes the best-fitting line based on Eq. (1). (b) The gravimetric moisture content vs. the calculated moisture contents. (c) The distribution of the difference between the gravimetric and the calculated moisture contents.

The intensity standard deviations (the error bars) indicated the fluctuations of the corrected intensities within the grid cell. A total of 55 samples (with a scanning distance $\leq$ 250 m) was adopted to quantify the surface moisture-corrected intensity relation. Because the point clouds at longer distances were too sparse, even no reflected points visible in some sampling positions. The corrected intensity gradually decreased with the increasing moisture contents from nearly dry (0%) to completely saturated (25%). By a least-square fitting, the parameters for $F_1(M)$ (Eq. (1)) were estimated as shown in Table 2, and the correlation-coefficient squared amounts to 0.92. Finally, the surface moisture contents in the sampling positions were derived from the point cloud data using Eq. (5). If the derived moisture contents were less than zero or higher than 26%, we set them to 0% (dry sand) and 26% (water surface), respectively.

As shown in Fig. 5b–c, the derived surface moisture contents from the point clouds in the sampling positions were compared with the gravimetric moisture contents. The majority of the derived moisture contents were very close to the gravimetric moisture contents. The relatively large deviations mainly occurred at the samples with the derived moistures > 20%. The possible reason is that these samples were scraped in the uneven ripple area where the crest and trough of ripples may have very distinct moisture values (Nield et al., 2011). This point is proven by the significant intensity standard deviations of these samples (Fig. 5a). Regardless of the sampling error in the ripple area, theoretically the proposed method can achieve a lower standard error of the derived moisture. Overall the standard error of all samples was around 2.27%, which outperformed the optical brightness methods (Edwards et al., 2013) and the methods using the TLSs of the visible wavelengths (Nield et al., 2014; Nield and Wiggs, 2011).

In addition, the intensity standard deviations of the field moisture samples were rather small with an average of 0.04, about 3% of the corrected intensity range. This suggested that the adopted method has a very high intensity resolution, and a potentially high moisture resolution (Nield et al., 2014; Nield and Wiggs, 2011; Nield et al., 2011). To prove the point further, we calculated the standard deviations of the derived moistures in each grid cell, which were also quite small with an average of 1.44% gravimetric moisture content. This is particularly noticeable in the samples with the derived moistures <20%, only with an average moisture standard deviation of 0.63%. It suggested that the proposed method is able to discriminate the moisture variation within 1% over low- and middle- beach surface moistures. This is important given that the aeolian sand transport is particularly sensitive to the changes in the lower moisture contents (Bauer et al., 2009; Namikas and Sherman, 1995; Nield and Wiggs, 2011).

It is noteworthy that the distribution of moisture contents of field samples is not uniform, mainly in the range of 0–1% and the range of 15–20%. This is since the samples were collected from the fixed sample

grid and that the sampling times were all during the low tide. Nevertheless, these moisture samples are sufficient to accurately model the relation of the beach surface moisture to the corrected intensity. Because the model adopted in this study is an exponential equation (Eq. (1)), where similar equations have been adopted in previous studies (Jin et al., 2020; Nield et al., 2014; Nolet et al., 2014; Smit et al., 2018; Tan et al., 2020). Before conducting the regression analysis, the exponential equation needs to be converted into a univariate linear equation by a logarithmic operation on two sides. For the regression analysis of the univariate linear equations, even though the distribution of the sample values is non-uniform, we still could get relatively accurate estimation results as long as possessing enough samples. By contrast, if the sample values were distributed discontinuously or non-uniformly for the high-order polynomial models, the obtained fitting curve could not be correct.

5. Application

5.1. Improved incidence angle calculation

To further investigate the suitability of the long-range TLS for monitoring the beach surface moisture dynamics, a hyper-temporal resolution case study (Eitel et al., 2016) across two tidal cycles was conducted (based on the obtained correction parameters in Section 4). However, unlike the short- and middle-range TLSs, it is difficult to calculate the incidence angles of the scanning points at a long distance due to the sparse point density for the long-range TLSs. In this study, the fitting radius to calculate the plane normal vectors of point clouds should be lower than 40 cm at least, considering the practical topography on the beach. Nonetheless, as shown in Fig. 2, the point density at distances exceeding 250 m was almost lower than 3 points within a 40 cm radius, which is not dense enough to derive accurate plane normal vectors. For this issue, the most common method is to expand the plane fitting radius if the beach topography is very flat or to perform measurements on the beach from multiple scanning positions.

In the present study, due to the scanner being permanently deployed on Ostend-Mariakerke beach for long-term continuous measurements, we proposed to replace the incidence angle of each TLS scanning point with the ones that were calculated based on the point clouds derived from the UAV images (acquired by a DJI Phantom 4 pro). The density of the point clouds derived from the UAV imagery is quite high, at least 100 points within a 40 cm search radius, and the average distance between the two point clouds is also very small: 3.86 ± 1.54 cm. Furthermore, the surface topography trend of both datasets was completely consistent. To prove the point further, we also compared the calculated incidence angles based on both sets of point cloud data (both acquired at 10:00 on April 17th, 2018). As shown in Fig. 6a, the comparison disregarded the
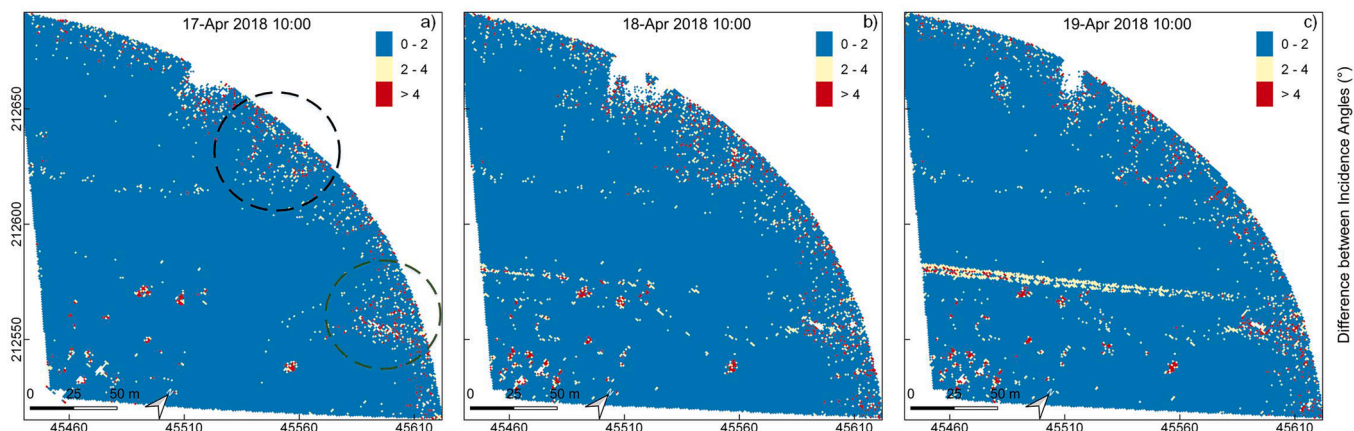
Fig. 6. The absolute difference between the calculated incidence angles based on the image-derived UAV point clouds (acquired at 10:00 on April 17th, 2018) and the incidence angles calculated based on the TLS point clouds acquired at (a) 10:00 on April 17th, 2018, (b) 10:00 on April 18th, 2018, and (c) 10:00 on April 19th, 2018, respectively. The black and green dotted lines denote the trough area and the sunken area of the upper-beach, respectively. (For interpretation of the references to color in this figure legend, the reader is referred to the web version of this article.)

point clouds with a distance >250 m to ensure a high accuracy and quality of the deriving plane normal vectors with a 40 cm fitting radius. Nevertheless, the selected area was still representative including all possible topography and surface properties of the beach, for example, the dry/wet sand area, the shallow waters, and the ripple area.

With the Fig. 2 analysis, the differences between the incidence angles mainly occurred in the low point density areas. In addition, the distribution of the large deviation (yellow and red points) was radiating, which was similar to the distribution of the point clouds with a low density in Fig. 2. The largest deviation occurred in the intertidal trough with very shallow waters and the sunken area of the upper-beach, where the point clouds had the lowest density. Generally, no points could be obtained by the TLS when the trough water reached a certain depth. Thus, it could be considered that if the TLS point clouds were dense enough, the differences between the incidence angles of the two datasets were quite small (≤2°).

As shown in Fig. 6b-c, we also compared the incidence angle of the image-derived point clouds with the incidence angle calculated using the TLS point clouds acquired on April 18th, 2018 (24 h later) and April 19th, 2018 (48 h later). The most noticeable change occurred at the dune edge, where the incidence angle deviation became larger over time due to the aeolian transport. Overall the difference of two datasets on the incidence angle was still quite small in 24 h. In the present study, we replaced the incidence angle of each TLS scanning point with the incidence angle of the corresponding horizontal nearest point in the image-derived point clouds. We chose the incidence angle of the nearest point

(rather than the mean of the neighboring points) because the image-derived point clouds kept a very high density in the full measuring area, and the average horizontal distance between the TLS points and the corresponding nearest points in the image-derived point clouds was only 2.66 ± 1.42 cm. It is noteworthy to explain that the incidence angles derived from the UAV images were repeatedly used during the two tidal cycles (24 h), considering no marked aeolian sand transport was observed during the largest part of the study period (see the wind data in Section 5.3). Human disturbance (e.g., footsteps and tire tracks) on the beach surface has been ignored.

5.2. Beach surface moisture content

The point cloud data were pre-processed using the MATLAB 2019b and CloudCompare v2.11 before calculating the beach surface moisture. The incidence angles were derived based on the image-derived point clouds with a plane-fitting of a 40 cm radius, and the beach surface moisture was calculated utilizing Eq. (5) and the parameters in Table 2. The negative, derived values were set to 0% denoting dry sand while the values higher than 26% were set to 26% denoting the shallow water surface. As shown in Fig. 7, the point cloud data were transferred to the rasters with a 1 × 1 m cell size. The beach elevation gradually decreased from the upper-beach (~7.5 m) to the low-tide line (~0 m). Before the correction, the original backscattered intensity strongly depended on the scanning distance and incidence angle. No significant intensity differences were observed in the long distance area (the right part of
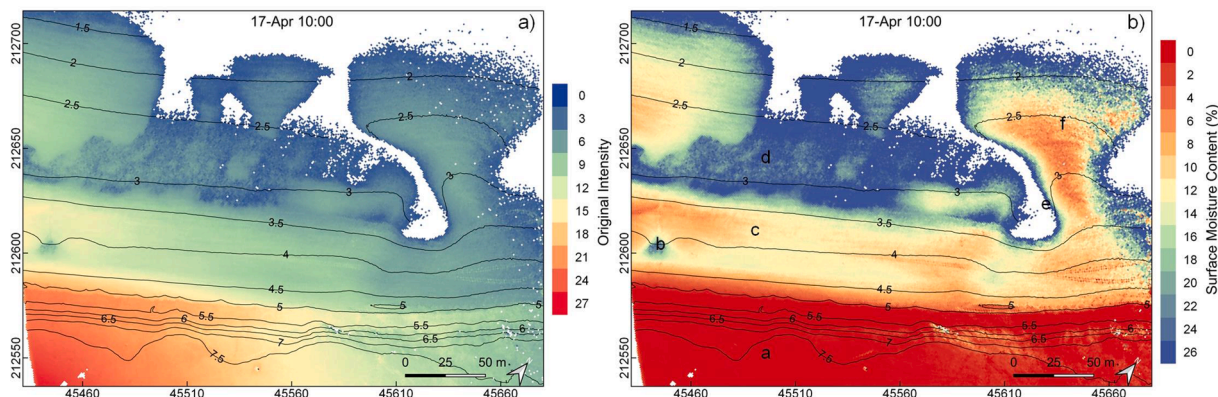

Fig. 7. (a) The TLS original intensity on the beach. (b) The beach surface moisture content after the intensity correction. The points a–f localize the sites of six close-up images.
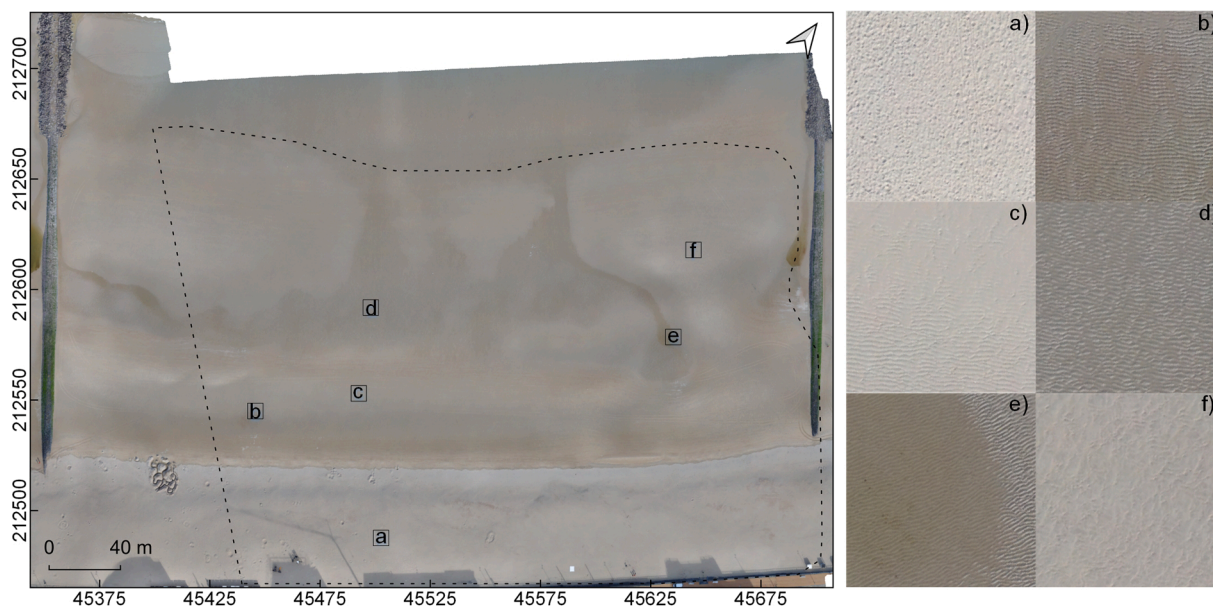
Fig. 8. The UAV-derived orthophoto of the study site (at 10:00 on April 17th, 2018) and the close-up images in the areas of a–f. The dotted line denotes the efficient measuring area of Riegl VZ-2000 TLS.
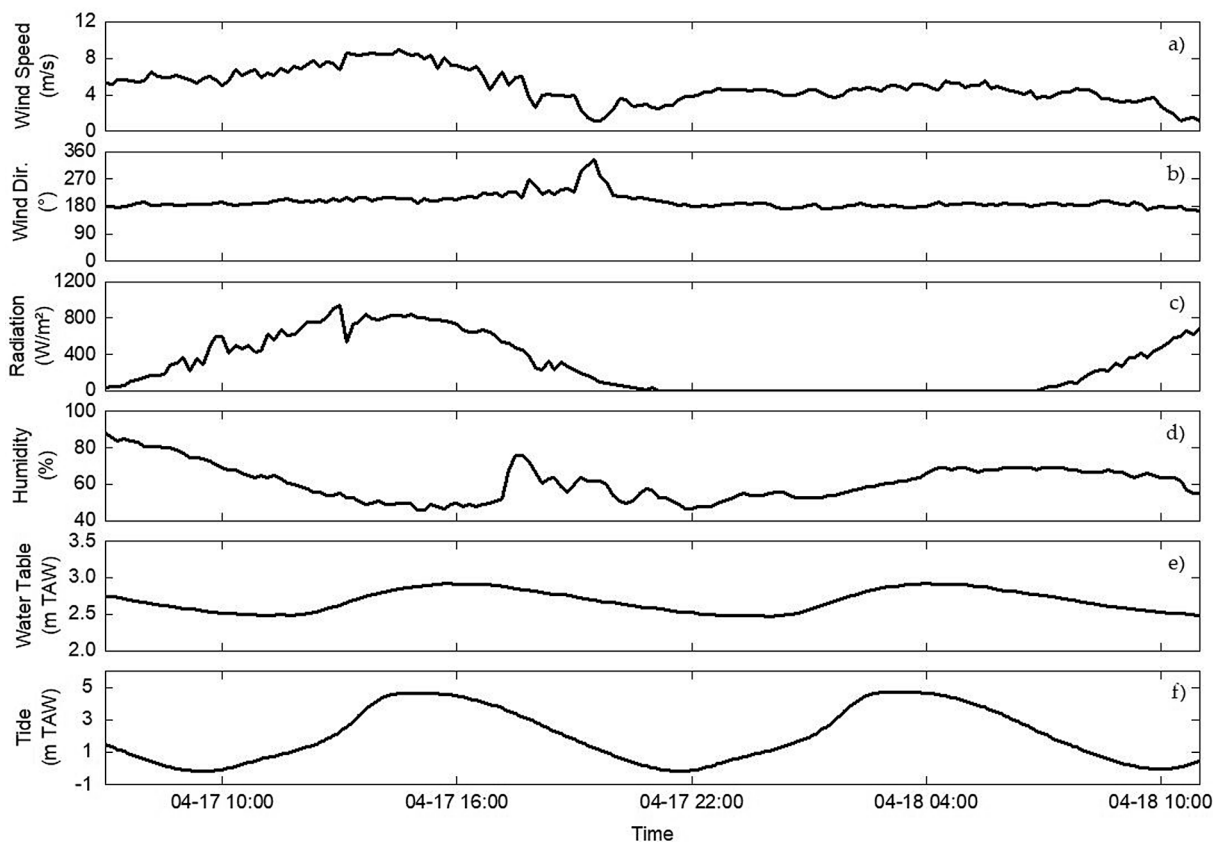

Fig. 9. The time series of the (a) wind speed, (b) wind direction, (c) solar radiation, (d) relative humidity, (e) groundwater table and (f) tidal elevation during the study period.

Fig. 7a), while in the upper-beach with similar surface properties, the original intensity varied significantly. Overall, the original intensity gradually decreased upon the increasing scanning distance and thus, it was difficult to distinguish the different moisture contents at a similar scanning distance.

After the correction, the original intensity was transferred to the beach surface moisture contents, which were independent of the scanning geometry. As shown in Fig. 7b, the highest moisture contents (blue points) were found at the edges along the blank area where no points were obtained (due to the shallow water). The variation in surface moisture in the long distance became very recognizable. In addition, the upper-beach also showed similar moisture contents (the dark red area).
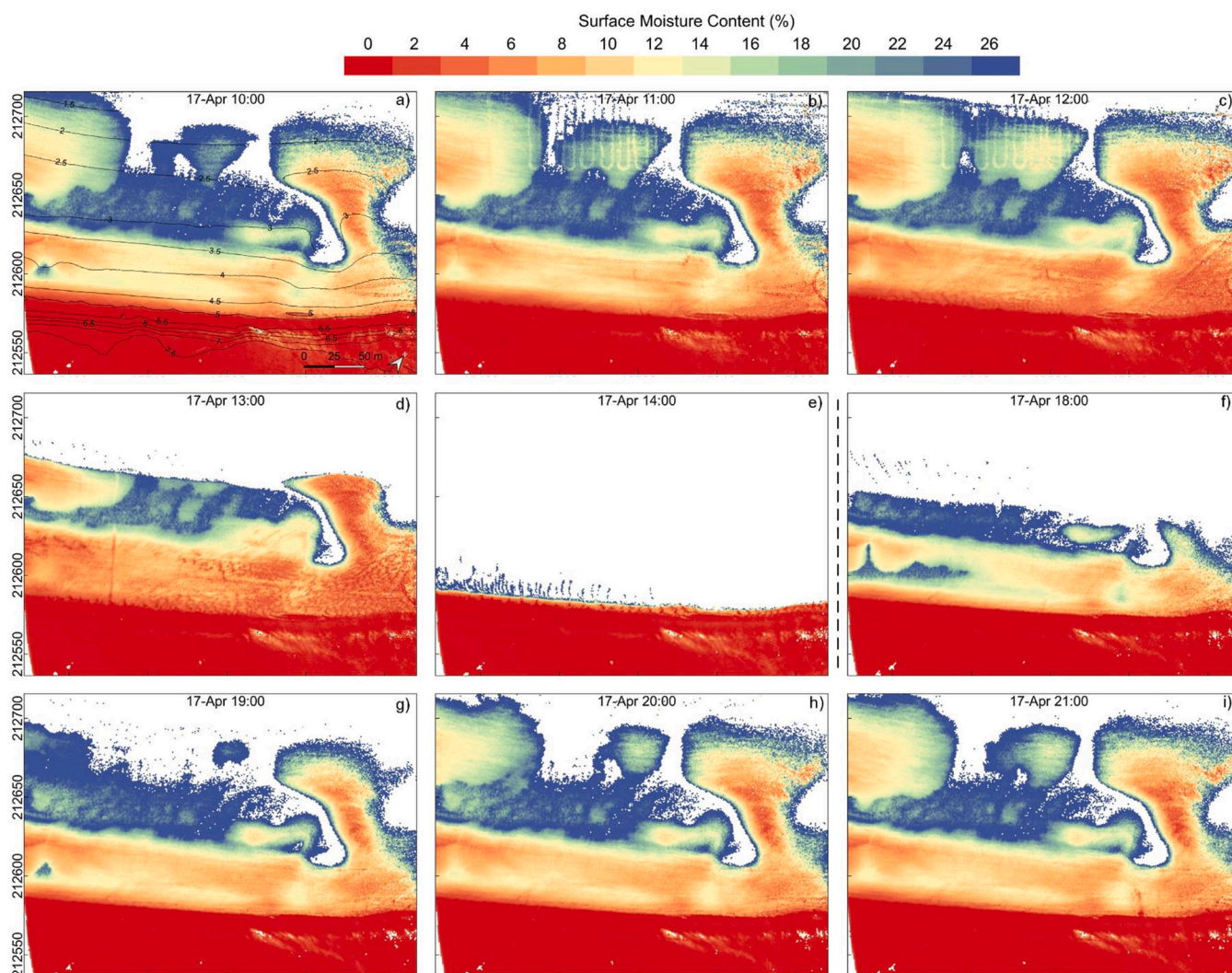
Fig. 10. The hourly surface moisture maps (1 × 1 m resolution) across two tidal cycles (24 h on April 17–18th, 2018) on Ostend-Mariakerke beach. The beach contour is shown in (a). The dashed lines denote the dividing line between the rising tide and falling tide period.

Evidently, the surface moisture contents were closely related to the beach surface elevation based on the shown contour line. The high elevation areas generally had lower surface moisture due to more time for water evaporation after the falling tide. In addition, the pore water in the high elevation areas would flow to the low elevation areas due to the gravity and infiltration (Tan et al., 2020). As a consequence, the details of the beach terrain became more intuitive and clear after correction. By comparing the derived beach surface moisture with the corresponding orthophoto (simultaneously taken on the study site) in Fig. 8, the derived moisture map could accurately describe the distribution of the dry sand area (dark red color) and the trough (dark blue color or blank area). Furthermore, slight variations in surface moisture could also be distinguished. For instance, the moisture variations in the transitional regions from the shallow water to the wet sand were completely consistent with the real moisture variations shown in the close-up images of Fig. 8b and 10e. This indicated the effectiveness and high accuracy of the derived surface moisture map.

5.3. Beach surface moisture dynamics

The hourly surface moisture maps (1 × 1 m resolution) across two tidal cycles (24 h on April 17–18th, 2018) are produced as an example application of the proposed method (Fig. 10). The atmospheric conditions, groundwater table and tidal elevation during the study period are displayed in Fig. 9 to help analyze how the beach surface moisture varies over space and time. On the whole, the atmospheric conditions were mild for the typical wind and wave climate on the Belgian coast. The wind speed kept below the threshold of the sand transport of 7 m/s (Montreuil et al., 2018) during most of the study period except for the period of 12:00–16:30 on April 17th, 2018, and the wind direction was also relatively stable, mainly being offshore (~180°). The air temperature remained at ~16 °C (not shown) and no precipitation was recorded during the study period. The solar radiation reached the highest value (936 w/m²) at 13:00, and the relative humidity reached the highest value (88%) in the morning. The groundwater table fluctuated over a range of 2.5 m to 3 m with respect to the TAW. The tidal elevation fell at approximately 10:00 and 22:00 and evidently, the groundwater table variation was closely related to the tidal elevation with a time lag of hours. In the afternoon of April 17th, 2018, a significant aeolian sand transport was observed on the beach.

As shown in Fig. 10, the hourly surface moisture maps clearly illustrate how the beach surface moisture fluctuates with the rising-falling tide during daytime and nighttime. From the upper-beach towards the sea, the surface moisture gradually increases from 0% to 25% with decreasing beach elevations, depicted with red, green, yellow and blue colors. No data points are visible in some intertidal troughs, while the
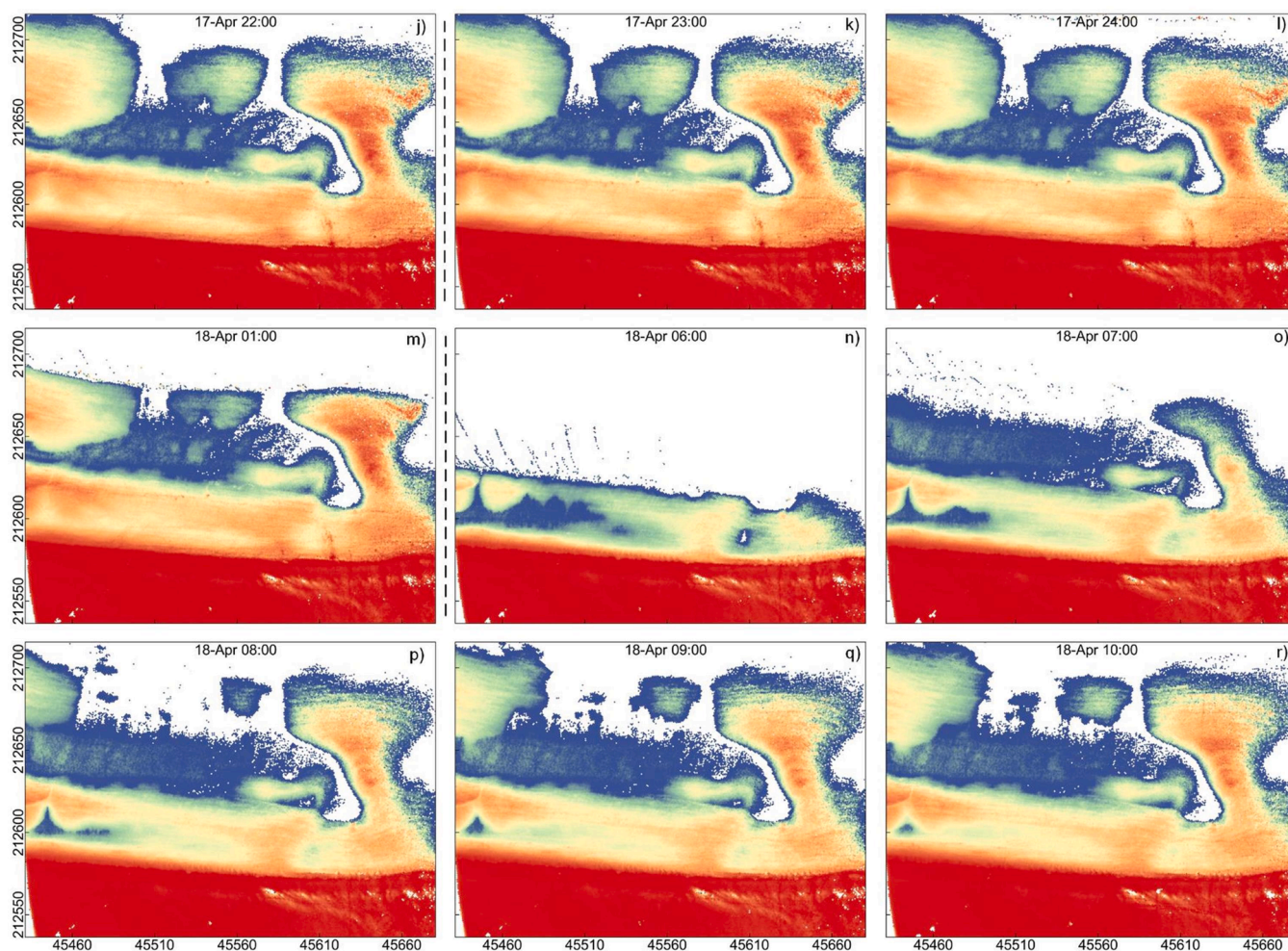
Fig. 10. (*continued*).

breaking waves in the surf zone are observed in several moisture maps. It is noteworthy that human disturbance, especially tire tracks, changed the original surface moisture in some areas of the beach (Fig. 10b–d). On the other hand, Fig. 11 visualizes the surface moisture differences between different moments during the low tide.

During the rising tide (Figs. 10a–e and 10j–m), the surface moisture above the high-water line (~4.8 m) remained relatively stable. In the intertidal zone, the surface moisture gradually decreased, and more scanning points became visible in the trough over time, until the beach was inundated again by the rising tide. The sandbar with relatively high elevations dried out faster than its surroundings. As shown in Fig. 11a (daytime), over two hours, the intertidal zone dries out with the largest part of moisture difference of 0% to –6.5% and the noticeable variation mainly occurred in the middle-high moisture area. By contrast, in Fig. 11c (nighttime), no significantly drying occurred in the intertidal zone (except at the edges of the trough). It is noteworthy that the surface moisture slightly (<2% moisture) increased during the night, especially in the dry upper-beach. The moist sea air and weak evaporation processes could contribute to this phenomenon.

Overall, the surface moisture in the intertidal zone gradually decreases in response to the rising tide and groundwater table before being inundated. This suggests that the evaporation dominated the surface moisture variations on the beach, while the groundwater table played a minor role. Especially during the daytime on April 17 (Fig. 10a–e and Fig. 11a), a combination of the solar radiation (~660 W/m^2) and wind (~7.1 m/s) contributed to a stronger evaporation process across the beach. Moreover, due to the wind blowing from the land, numerous dry

sands were blown from the dune to the intertidal zone, so the surface moisture in the intertidal zone dried out faster. As shown in Fig. 10c-d, numerous dry sand ripples blown from the dune were visible in the upper intertidal zone. Theoretically, if the groundwater table remains close to the beach surface to some extent, it would influence the surface moisture contents (Namikas et al., 2010). Based on the study in (Montreuil et al., 2018), the capillary fringe should be between 22 and 26 cm (calculated based on the sediment sizes of the beach) above the groundwater table. Here, the groundwater table fell below the range of the capillary fringe from the beach surface on the upper-beach and upper intertidal zone (with elevations higher than ~3.3 m). Thus, its effect on the surface moisture was limited in these areas. Because the groundwater table under the intertidal zone is generally lower than the water level under the upper-beach (where the dipwell was installed), it is possible that a larger beach area was only little affected by the groundwater table.

During the falling tide (Fig. 10f–j and 10n–r), the surface moisture dynamics significantly differed from the rising tide period. Above the high-water line, the surface moisture remained relatively stable. The saturated areas on the upper intertidal zone became smaller and large areas of data points close to the sea became visible over time. Overall, the surface moisture in the intertidal zone decreased faster during the falling tide due to both the gravitational drainage associated with the falling groundwater table and the evaporation process through the solar radiation and wind. More intuitive variations were demonstrated in Fig. 11d (daytime): over two hours, the intertidal zone dries out with the largest part of moisture difference of 0% to –4% and the large variation
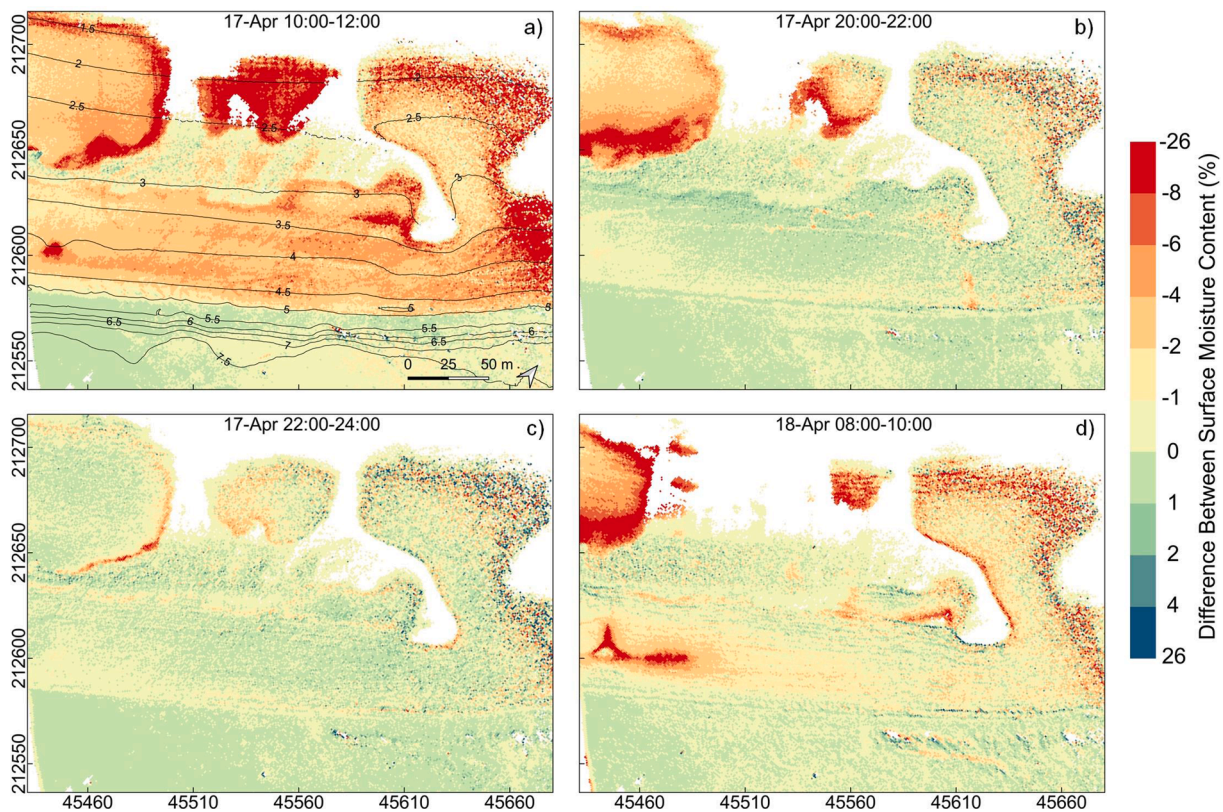
Fig. 11. The beach surface moisture variations between different moments during low tide. (a) and (c) occurred in the rising tide period. (b) and (d) took place during falling tide.

mainly occurred in the high moisture areas. In Fig. 11b (nighttime), the surface moisture variation is similar to the daytime, but the area of moisture increasing (~1%) was significantly larger than the area in the daytime, due to the lack of solar radiation. Overall, the rate of drying out was closely related to the initial moisture on the beach surface. The saturated area generally dried out at the highest rate, while the low moisture area (especially the dry upper-beach) could become moister due to the moist sea air and weak evaporation process at night.

During the study period, the distribution of the beach surface moisture varied significantly over space and time, under the synthetic effect of the beach terrain, tide elevation, groundwater table, evaporation and precipitation, etc. Thus, the distribution of beach surface moisture is very difficult to parameterize. Previous studies stated that the beach surface moisture higher than 10% could prohibit the aeolian sand transport entirely, while the sand with surface moisture contents lower than 4% is always available for aeolian sand transport (Delgado-Fernandez and Davidson-Arnott, 2011; Smit et al., 2019). Our surface moisture maps could provide accurate and intuitive information about which part of the beach is potentially exposed to aeolian sand transport. Consistent with previous studies (Bauer et al., 2009; Brakenhoff et al., 2019; Namikas et al., 2010; Smit et al., 2019), Fig. 10 demonstrates that the spatial surface moisture variations on the beach could be conceptualized to three zones: (1) the dry upper-beach above the high-water line, where the surface moisture < ~2% and the moisture variations are very low over time; (2) the upper intertidal zone (with elevations of ~3.3–4.8 m) and the sandbar in the lower intertidal zone, where the surface moisture could vary strongly in the range of ~4–26% with the rising-falling tide (26% denoting the water surface). Thus, the sand in this area has a chance for aeolian transport. However, the intertidal trough could prohibit the sand blown from the sandbars to reach the foredunes (Anthony et al., 2009); (3) the wet zones in the lower intertidal zone (with elevations < ~3.3 m) including the trough, where the surface moisture always remains at ~18–26%. The sand in this area is

too wet to be entrained by the wind.

6. Conclusion

This study shows a new high-resolution remote sensing method to monitor the spatiotemporal variation in surface moisture on a sandy beach using a long-range static TLS (Riegl VZ-2000). Considering the effect of the target surface roughness on the intensity and the laboratory's length limitation, a new intensity correction method is proposed, which only uses the field point cloud data measured on a homogenous beach surface without time-consuming indoor experiments. The relation of beach surface moisture contents to the corrected intensity was modeled by an exponential function with a correlation-coefficient squared of 0.92. Combining the exponential model and the intensity correction model, the authors developed a moisture estimation model which could directly derive the beach surface moisture from the original intensity of the TLS. The standard error is 2.27%, which outperforms the optical brightness methods and the methods using the TLSs of the visible wavelengths. In addition, the average standard deviation of the derived moistures (in the 1×1 m grid cell) is about 0.63% under the derived moistures < 20%. It showed that the adopted method has the ability to discriminate the moisture variation within 1% over low- and middle- beach surface moistures.

Based on the proposed moisture estimation model, the hourly beach surface moisture maps (1×1 m resolution) were produced and the surface moisture dynamics across two tidal cycles on the beach was investigated, combined with the information on the atmospheric conditions, groundwater table and tidal elevation during the period. Due to the sparse point cloud density at long distances, our study improved the calculation accuracy of the incidence angles at long distances using the point cloud data derived from the corresponding UAV images. The derived surface moisture maps indicate that the proposed moisture estimation model could effectively eliminate the effect of scanning

geometry on the original backscattered intensity and accurately describe the beach surface moisture dynamics. Currently, a major shortcoming for developing a more accurate aeolian sand transport model is the lack of suitable methods to monitor the surface moisture dynamics (daytime and nighttime) over a substantial beach section (hundreds of meters) at a high frequency (minutes to hours). The proposed method is a highly suitable solution, which could not only be applied to derive the beach surface moisture but also to study the changes in beach morphology and dune volume at a high spatial and temporal resolution. Future studies are recommended to improve the prediction model for the aeolian sand transport using the derived beach surface moisture based on the proposed method.

Declaration of Competing Interest

The authors declare that they have no known competing financial interests or personal relationships that could have appeared to influence the work reported in this paper.

Appendix A. Supplementary data

Supplementary data to this article can be found online at https://doi. org/10.1016/j.isprsjprs.2021.01.011.

References

Anthony, E.J., Ruz, M.-H., Vanhée, S., 2009. Aeolian sand transport over complex intertidal bar-trough beach topography. Geomorphology 105 (1–2), 95–105.

Atherton, R.J., Baird, A.J., Wiggs, G.F., 2001. Inter-tidal dynamics of surface moisture content on a meso-tidal beach. Journal of Coastal Research 482–489.

Bauer, B., Davidson-Arnott, R., Hesp, P., Namikas, S., Ollerhead, J., Walker, I., 2009. Aeolian sediment transport on a beach: Surface moisture, wind fetch, and mean transport. Geomorphology 105 (1–2), 106–116.

Brakenhoff, L.B., Smit, Y., Donker, J.J., Ruessink, G., 2019. Tide-induced variability in beach surface moisture: Observations and modelling. Earth Surface Processes and Landforms 44 (1), 317–330.

Coast, F.A.f.M.S.a., 2020. Meetnet Vlaamse Banken, Available from: https:// meetnetvlaamsebanken.be/.

Darke, I., Davidson-Arnott, R., Ollerhead, J., 2009. Measurement of beach surface moisture using surface brightness. Journal of Coastal Research 248–256.

Davidson-Arnott, R.G., Yang, Y., Ollerhead, J., Hesp, P.A., Walker, I.J., 2008. The effects of surface moisture on aeolian sediment transport threshold and mass flux on a beach. Earth Surface Processes and Landforms: The Journal of the British Geomorphological Research Group 33 (1), 55–74.

De Sloover, L., De Wulf, A., Stal, C., Verbeurgt, J., Vos, S., 2019. Case Study of a Hypertemporal Terrestrial LiDAR to Monitor a Macrotidal Beach: Assessment of Different Calibration Procedures. International Multidisciplinary Scientific GeoConference: SGEM 19 (2.2), 57–64.

Delgado-Fernandez, I., 2011. Meso-scale modelling of aeolian sediment input to coastal dunes. Geomorphology 130 (3–4), 230–243.

Delgado-Fernandez, I., Davidson-Arnott, R., 2011. Meso-scale aeolian sediment input to coastal dunes: The nature of aeolian transport events. Geomorphology 126 (1–2), 217–232.

Deronde, B., Houthuys, R., Henriet, J.P., Lancker, V.V., 2008. Monitoring of the sediment dynamics along a sandy shoreline by means of airborne hyperspectral remote sensing and LIDAR: a case study in Belgium. Earth Surface Processes and Landforms: The Journal of the British Geomorphological Research Group 33 (2), 280–294.

Edwards, B.L., Namikas, S.L., 2009. Small-scale variability in surface moisture on a fine-grained beach: implications for modeling aeolian transport. Earth Surface Processes and Landforms 34 (10), 1333–1338.

Edwards, B.L., Schmutz, P.P., Namikas, S.L., 2013. Comparison of surface moisture measurements with depth-integrated moisture measurements on a fine-grained beach. Journal of Coastal Research 29 (6), 1284–1291.

Eitel, J.U., Höfle, B., Vierling, L.A., Abellán, A., Asner, G.P., Deems, J.S., Glennie, C.L., Joerg, P.C., LeWinter, A.L., Magney, T.S., 2016. Beyond 3-D: The new spectrum of lidar applications for earth and ecological sciences. Remote Sensing of Environment 186, 372–392.

Fang, W., Huang, X., Zhang, F., Li, D., 2015. Intensity correction of terrestrial laser scanning data by estimating laser transmission function. IEEE Transactions on Geoscience and Remote Sensing 53 (2), 942–951.

Haerens, P., Bolle, A., Trouw, K., Houthuys, R., 2012. Definition of storm thresholds for significant morphological change of the sandy beaches along the Belgian coastline. Geomorphology 143, 104–117.

Jin, J., De Sloover, L., Verbeurgt, J., Stal, C., Deruyter, G., Montreuil, A.-L., De Maeyer, P., De Wulf, A., 2020. Measuring Surface Moisture on a Sandy Beach based on Corrected Intensity Data of a Mobile Terrestrial LiDAR. Remote Sensing 12 (2), 209.

Kaasalainen, S., Hyyppa, H., Kukko, A., Litkey, P., Ahokas, E., Hyyppa, J., Lehner, H., Jaakkola, A., Suomalainen, J., Akujarvi, A., 2009. Radiometric calibration of LIDAR intensity with commercially available reference targets. IEEE Transactions on Geoscience and Remote Sensing 47 (2), 588–598.

Kaasalainen, S., Jaakkola, A., Kaasalainen, M., Krooks, A., Kukko, A., 2011. Analysis of incidence angle and distance effects on terrestrial laser scanner intensity: Search for correction methods. Remote Sensing 3 (10), 2207–2221.

Keijsers, J., De Groot, A., Riksen, M., 2016. Modeling the biogeomorphic evolution of coastal dunes in response to climate change. Journal of Geophysical Research: Earth Surface 121 (6), 1161–1181.

Kukko, A., Kaasalainen, S., Litkey, P., 2008. Effect of incidence angle on laser scanner intensity and surface data. Applied Optics 47 (7), 986–992.

Kuschnerus, M., Lindenbergh, R., Vos, S., 2020. Coastal Change Patterns from Time Series Clustering of Permanent Laser Scan Data. Earth Surface Dynamics Discussions 1–29.

McKenna Neuman, C., Langston, G., 2006. Measurement of water content as a control of particle entrainment by wind. Earth Surface Processes and Landforms: The Journal of the British Geomorphological Research Group 31 (3), 303–317.

Montreuil, A.-L., Chen, M., Brand, E., Strypsteen, G., Rauwoens, P., Vandenbulcke, A., De Wulf, A., Dan, S., Verwaest, T., 2018. Dynamics of Surface Moisture Content on a Macro-tidal Beach. Journal of Coastal Research 85 (sp1), 206–210.

Namikas, S., Edwards, B., Bitton, M., Booth, J., Zhu, Y., 2010. Temporal and spatial variabilities in the surface moisture content of a fine-grained beach. Geomorphology 114 (3), 303–310.

Namikas, S.L., Sherman, D.J., 1995. A review of the effects of surface moisture content on aeolian sand transport. Desert aeolian processes. Springer 269–293.

Nield, J.M., King, J., Jacobs, B., 2014. Detecting surface moisture in aeolian environments using terrestrial laser scanning. Aeolian Research 12, 9–17.

Nield, J.M., Wiggs, G.F., 2011. The application of terrestrial laser scanning to aeolian saltation cloud measurement and its response to changing surface moisture. Earth Surface Processes and Landforms 36 (2), 273–278.

Nield, J.M., Wiggs, G.F., Squirrell, R.S., 2011. Aeolian sand strip mobility and protodune development on a drying beach: examining surface moisture and surface roughness patterns measured by terrestrial laser scanning. Earth Surface Processes and Landforms 36 (4), 513–522.

Nolet, C., Poortinga, A., Roosjen, P., Bartholomeus, H., Ruessink, G., 2014. Measuring and modeling the effect of surface moisture on the spectral reflectance of coastal beach sand. PloS one 9 (11), e112151.

Oblinger, A., Anthony, E.J., 2008. Surface moisture variations on a multibarred macrotidal beach: implications for aeolian sand transport. Journal of Coastal Research 1194–1199.

Philpot, W., 2010. Spectral reflectance of wetted soils. Proceedings of ASD and IEEE GRS 2, 1–12.

Ruessink, G., Brakenhoff, L., van Maarseveen, M., 2014. Measurement of surface moisture using infra-red terrestrial laser scanning. EGUGA 2797.

Smit, Y., Donker, J.J., Ruessink, G., 2019. Spatiotemporal surface moisture variations on a barred beach and their relationship with groundwater fluctuations. Hydrology 6 (1), 8.

Smit, Y., Ruessink, G., Brakenhoff, L.B., Donker, J.J., 2018. Measuring spatial and temporal variation in surface moisture on a coastal beach with a near-infrared terrestrial laser scanner. Aeolian Research 31, 19–27.

Stone, M.H., 1948. The generalized Weierstrass approximation theorem. Mathematics Magazine 21 (5), 237–254.

Tan, K., Chen, J., Qian, W., Zhang, W., Shen, F., Cheng, X., 2019. Intensity Data Correction for Long-Range Terrestrial Laser Scanners: A Case Study of Target Differentiation in an Intertidal Zone. Remote Sensing 11 (3), 331.

Tan, K., Chen, J., Zhang, W., Liu, K., Tao, P., Cheng, X., 2020. Estimation of soil surface water contents for intertidal mudflats using a near-infrared long-range terrestrial laser scanner. ISPRS Journal of Photogrammetry and Remote Sensing 159, 129–139.

Tan, K., Cheng, X., 2015. Intensity data correction based on incidence angle and distance for terrestrial laser scanner. Journal of Applied Remote Sensing 9 (1), 094094.

VLIZ, F.M.I., 2020. Crest project, Available from: http://www.crestproject.be/en.

Vos, S., Lindenbergh, R., de Vries, S., Aagaard, T., Deigaard, R., Fuhrman, D., 2017. Coastscan: Continuous monitoring of coastal change using terrestrial laser scanning. Proceedings of the Coastal Dynamics.

Wiggs, G., Baird, A., Atherton, R., 2004. The dynamic effects of moisture on the entrainment and transport of sand by wind. Geomorphology 59 (1–4), 13–30.

Yang, Q., Snyder, J., Tobler, W., 2020. Map projection transformation: principles and applications. CRC Press 28–32.

Yang, X., Yu, Y., Li, M., 2019. Estimating soil moisture content using laboratory spectral data. Journal of Forestry Research 30 (3), 1073–1080.

Zámečníková, M. and Neuner, H., 2017. Investigation of the distance dependence of the combined influence of the incidence angle and the surface roughness on the reflectorless distance measurement of a scanning total station. Allgemeine Vermessungs-Nachrichten (AVN) begutachtete Beiträge, 124(11-12): 353-361.